

Power-to-methane via co-electrolysis of H₂O and CO₂: The effects of pressurized operation and internal methanation[☆]

Ligang Wang^{a,b,*}, Megha Rao^c, Stefan Diethelm^a, Tzu-En Lin^d, Hanfei Zhang^e, Anke Hagen^c, François Maréchal^b, Jan Van herle^a

^a Group of Energy Materials, Swiss Federal Institute of Technology in Lausanne, Switzerland

^b Industrial Process and Energy Systems Engineering, Swiss Federal Institute of Technology in Lausanne, Switzerland

^c Department of Energy Conversion and Storage, Technical University of Denmark, Denmark

^d Institute of Biomedical Engineering, National Chiao Tung University, Taiwan, ROC

^e Department of Energy, Systems, Territory and Constructions Engineering, University of Pisa, Italy



HIGHLIGHTS

- Internal methanation effectively promoted by high pressure and reactant utilization.
- Stack outlet CH₄ fraction up to 30 vol.% at 0.3 A/cm² and large stack cooling.
- Stack outlet CH₄ fraction only up to 15 vol.% to achieve high system efficiency.
- Internal methanation as internal heat source preferred by endothermic operation.

ARTICLE INFO

Keywords:

Energy storage
Power-to-methane
Solid-oxide electrolyzer
Co-electrolysis
CO₂ utilization
Pressurized operation
Internal methanation

ABSTRACT

This paper presents a model-based investigation to handle the fundamental issues for the design of co-electrolysis based power-to-methane *at the levels of both the stack and system*: the role of CO₂ in co-electrolysis, the benefits of employing pressurized stack operation and the conditions of promoting internal methanation. Results show that the electrochemical reaction of co-electrolysis is dominated by H₂O splitting while CO₂ is converted via reverse water-gas shift reaction. Increasing CO₂ feed fraction mainly enlarges the concentration and cathode-activation overpotentials. Internal methanation in the stack can be effectively promoted by pressurized operation under high reactant utilization with low current density and large stack cooling. For the operation of a single stack, methane fraction of dry gas at the cathode outlet can reach as high as 30 vol.% (at 30 bar and high flowrate of sweep gas), which is, unfortunately, not preferred for enhancing system efficiency due to the penalty from the pressurization of sweep gas. The number drops down to 15 vol.% (at 15 bar) to achieve the highest system efficiency (at 0.27 A/cm²). The internal methanation can serve as an effective internal heat source to maintain stack temperature (thus enhancing electrochemistry), particularly at a small current density. This enables the co-electrolysis based power-to-methane to achieve higher efficiency than the steam-electrolysis based (90% vs 86% on higher heating value, or 83% vs 79% on lower heating value without heat and converter losses).

1. Introduction

European Union has set the goal of reducing greenhouse gases by 80% in 2050 from 1990 [1], for which the use of renewable energy sources will play a significant role, particularly, in the power-generation sector. A new record of wind-power utilization has been set in

Denmark with 43.6% of its total power consumption supported by wind turbines in 2017 [2]. The contribution of renewable energy sources to electricity consumption is expected to be 30% in the European Union and 50% in Denmark by 2030 [3].

The high penetration of intermittent renewable energy sources requires large-scale energy storage, e.g., pumped-hydro, compressed-air

[☆] The short version of the paper was presented at ICAE2018, Aug 22–25, Hong Kong, but was not published in the conference proceedings. This paper is a substantial extension of the short version of the conference paper.

* Corresponding author at: Group of Energy Materials and Group of Industrial Process and Energy Systems Engineering, Swiss Federal Institute of Technology in Lausanne (EPFL), Switzerland.

E-mail addresses: lgwangeao@163.com, ligang.wang@epfl.ch (L. Wang).

<https://doi.org/10.1016/j.apenergy.2019.05.098>

Received 29 December 2018; Received in revised form 20 April 2019; Accepted 7 May 2019

Available online 16 May 2019

0306-2619/© 2019 The Authors. Published by Elsevier Ltd. This is an open access article under the CC BY-NC-ND license (<http://creativecommons.org/licenses/by-nc-nd/4.0/>).

Nomenclature**Abbreviations**

CE	co-electrolysis
DGM	dusty gas model
HEN	heat exchanger network
HHV	high heating value
LHV	lower heating value
LSCF	(La,Sr)(Co,Fe) O _{3-δ}
MILP	mixed-integer linear programming
MINLP	mixed-integer nonlinear programming
OCV	open circuit voltage
PtM	power-to-methane
RWGS	reverse water-gas shift reaction
SE	steam electrolysis
SMRR	steam-methane reforming reaction
SOE	solid-oxide electrolyzer/electrolysis
SRU	serial repeating unit
TPB	triple phase boundary
UF	utilization factor
WGS	water-gas shift reaction
YSZ	Yttria-stabilized zirconia

Mathematical Symbols

β	asymmetry charge-transfer co-efficient, –
ΔH	enthalpy of reaction
δ	thickness, m
\dot{E}	energy flow, GJ/h
\dot{Q}	energy loss, GJ/h
\dot{F}	molar flowrate, kmol/h
$\dot{n}_{eq,i_{rxn}}$	extent of reaction i_{rxn} , kmol/h
\dot{N}_i	molar fraction of species i , mol/s/m ²
\dot{r}	reaction rate, kmol/h/m ³
ϵ	porosity, –
Γ	surface site density, mol/m ²
γ	sticking coefficient, –
μ	viscosity coefficient, Pa s
Ω	dimensionless diffusion collision integral, –
ω	molar flowrate, kmol/h
$\bar{M}_{i,j}$	average molecular weight of binary mixture, g/kmol
σ	mean characteristic length, –
τ	tortuosity, –
ε	average Lennard-Jones characteristic length, –
B	permeability, m ²
$c_{i_{rxn},i}$	stoichiometry coefficient of the species i for the reaction i_{rxn} , –

d_p	particle diameter, m
$D_{Kn,i}^{eff}$	effective Knudsen diffusion coefficient of species i , m ² /s
$D_{i,j}^{eff}$	effective binary diffusion coefficient of the species i and j , m ² /s
E	activation energy, J/mol
h	molar specific enthalpy, GJ/kmol
J	current density, A/cm ²
J_0, J^*	exchange current density, A/cm ²
k	pre-exponential factor, physical units varied
L	length, m
M	molecular weight, g/kmol
n	the number of species, –
p	total gas pressure, Pa
p^*	saturation pressure, bar
R	universal gas constant, J/mol/K
r_g	pore radius, m
T_C	temperature, °C
T_K	temperature, K
V	voltage, V
Z	molar fraction, –
F	Faraday constant, 9.6485e4 C/mol

Superscripts

0	gas channel-electrode surface
her, HER	hydrogen evolution reaction
oer, OER	oxygen evolution reaction
TPB	triple phase boundary

Subscripts

i, j	species index
i_{rxn}	reaction index
act	activation
d	desorption
e	electrolyte
ec	electrochemical
elec	electricity
gc	gas channel
her, HER	hydrogen evolution reaction
in	inlet
loss	loss
mic	metallic interconnect
nernst	nernst
oer, OER	oxygen evolution reaction
ohm	ohmic
tot	total

energy storage [4,5], flow battery [6] and chemical storage. The storage of hydrogen and derived chemicals, e.g., ammonia and methane, is regarded as the only viable option for electricity storage at a scale of over 10 GWh [7]. Methane storage is particularly advantageous due to the existing, large-scale infrastructure. The available capacity of methane storage has been reported to be over 1100 TWh, equivalent to 1/3 of the yearly power generation or the total yearly renewable power generation in Europe [8]. It is also mentioned that the natural-gas consumption illustrates stronger seasonal variation than the use of electricity, and electricity alone will not be able to meet peak energy demand unless massive additional investments are made into power infrastructure [8]. Considering that natural-gas transmission infrastructure is on average 10 times cheaper than power lines/cables [8], methane storage seems to be the most promising means of large-scale seasonal energy storage.

Converting electricity to methane, namely power-to-methane (PtM), is mostly achieved by combining electrolysis and methanation. Compared with low-temperature alkaline or proton-exchange-membrane electrolyzers, high-temperature solid-oxide electrolyzer (SOE) enables high-efficient PtM conversion with the advantages of (1) high electrolysis (electrical) efficiency, (2) the ability of co-electrolysis (CE) of CO₂ and H₂O to produce syngas with suitable composition for downstream chemical synthesis [9], and (3) thermal coupling between the methanator and electrolyzer [10]. At the cell and stack levels, the design and manufacturing of cell and stack continue to be improved in order to enhance the performance, durability and scalability. For example, a Danish project, *Towards Solid Oxide Electrolysis Plants in 2020*, has demonstrated the durability of such cells under high current density implying the stability and performance of state-of-the-art SOE [3]. The BALANCE project [11] aims at demonstrating the use of the SOE for

grid balancing with real-time simulated wind profiles. The ECo project [12] focused on the improvement of the SOE cell for CE operation considering various impurities in different CO₂ sources. The capacity of a single electrolyzer stack is currently between 3 and 15 kW. The kW-level stacks can be assembled to stack modules to build large plants in a similar fashion as the largest commercial solid-oxide fuel cell plant [13] (250 kW) based on 1 kW stack. The 100–200 kW fuel-cell stack modules are under development by several companies. Enlarging the capacity of a single stack might be more effective for scale-up. The stacks of 6–25 kW at fuel cell mode or 20–75 kW at electrolyzer mode have been or soon become available thanks to, e.g., SOLIDpower [14] and Sunfire [15]. These large-capacity stack concepts might facilitate the scale-up of SOE plants to several MW-level and higher. At the system level, methanation heat can be used to generate steam for the SOE, which is investigated by several projects. The HELMETH project [16] was supposed to demonstrate the coupling under pressurized conditions with an overall system efficiency of 76% (based on a higher heating value, HHV) [17]. The PENTAGON project [18] proposed to demonstrate a small-scale plant by using intermediate heat transfer fluid (thermal oil) to realize such thermal coupling. The system design via steam electrolysis (SE) performed and compared for different stack operating points showed a maximum achievable efficiency of 85% (HHV) at 700 °C (stack inlet temperature) and 26 bar [19].

On the system design and operation of SOE-based PtM plants, there are still some fundamental issues not sufficiently addressed in the literature, particularly, for the cases with CE, where methane can be produced inside the stack via the so-called internal methanation in the presence of nickel:

- is it beneficial to operate the stack under pressurized conditions?
- which conditions are preferred by internal methanation and is it beneficial at the system level?

At the cell and stack level, it has been observed in [20–22] that the pressurized operation of the SOE leads to (1) an increased open circuit voltage (OCV) and an enhanced mass diffusion to relieve local reactant shortage occurring at high reactant utilization [22], which reduces the increased concentration overpotential caused by the lack of reactants, and (2) an increased internal methane production for CE [23], since the outlet gas of the SOE is close to chemical equilibrium [22]. Recently, a stack tested at 18.7 bar and 700 °C showed a significant internal methane production, 18 vol.% of dry gas at the cathode outlet [24]. From the system viewpoint, pressurized stack operation might be energetically favored [25]; however, this might be only true for specific design points, e.g., at a low current density. The systematic

investigation on the effects of various operating variables has been performed by the authors in [26]; however, the study was based on a stack model without considering the internal methanation at the cathode side, which could bias the conclusions obtained there.

With such contexts, this paper aims at answering the above two critical questions from both the stack and system levels via process system engineering methodologies. The main tasks include:

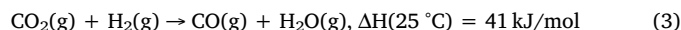
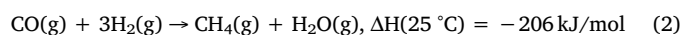
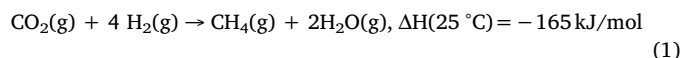
- develop a procedure to automatically identify feasible, practical stack operating/design points,
- identify the conditions to maximize methane production at the stack level, and
- investigate the effects of pressurized operation and the benefits of internal methanation at the system level

The remaining of the paper is organized as follows: In Section 2, the system concept of the investigated PtM is introduced by emphasizing catalytic methanation and reactor concepts (Section 2.1). Then, process modeling is handled in Section 3 with detailed mathematical formulations of the SOE (Section 3.1.2), the procedures for model calibration (Section 3.1.3), and the identification of feasible operating points (Section 3.1.4). Afterwards, the methodology employed to the system design at a conceptual level is given in Section 4. The results are further discussed in Section 5 to answer the aforementioned two research questions, which are then concluded in Section 6.

2. Power-to-methane via co-electrolysis of H₂O and CO₂

2.1. Catalytic methanation and reactor concepts

For the methanation of CO₂ (200–550 °C, 5–30 bar), thermodynamic fundamentals have been intensively discussed elsewhere, e.g., [27–29]. The active reactions involved are CO₂ methanation (Eq. (1)), CO methanation (Eq. (2)) and reverse water-gas shift reaction (RWGSR, Eq. (3)):



The limiting factors for methanation reactions are the kinetics at a low temperature and chemical equilibrium at a high temperature [26,28]. Therefore, the literature focused on catalysts (e.g., Ni or Ru

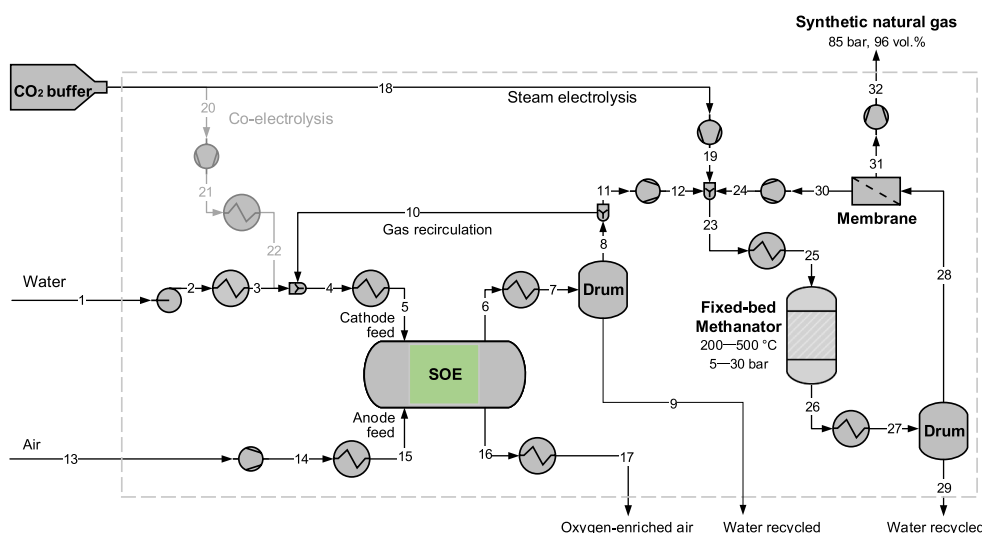


Fig. 1. Schematic of SOE-based power-to-methane system with air as the sweep gas (adjusted from [26]). The system boundary for this investigation is represented by the dashed rectangular. Heat exchanger network is not explicitly designed but its performance is estimated with classical chemical engineering method in, e.g., [39]. The membrane module is sized to achieve a methane purity (over 96 vol.%) for gas-grid injection. For the purpose of this paper, the purge stream for the recirculation loop of the methanation subsystem to avoid the accumulation of inert species is not considered, since it does not affect largely the system efficiency and methane yield for the presented conceptual system.

with Al_2O_3 or TiO_2 bases [27]) and reaction mechanisms (e.g., [30–33]), and design/operation single reactor (e.g., [34]) and reactor systems (e.g., [16,28,35]) for the enhancement of heat and mass transfer to control peak temperature and achieve high conversion. Many concepts for catalytic methanators are available [35], e.g., isothermal or adiabatic fixed-bed, fluidized-bed, or structured (honeycomb, micro-channel or sorption enhanced) reactors. Adiabatic fixed-bed reactors are the most mature with low complexity and high flexibility; however, due to the exothermic methanation reactions and fast kinetics, the peak temperature of the reactor may reach as high as 700 °C immediately after the reactions start [36], which can significantly limit the single-pass conversion. Therefore, adiabatic fixed-bed concepts usually connect 2–5 reactors in series [28,35] with water knock-out in between to promote the reaction towards methane production. To reduce the system complexity and enhance single-pass conversion, (quasi-) isothermal reactor concepts are under investigation as described in [16,34] with various schemes, e.g., staged CO_2 feed [28] and different cooling schemes [37,38]. However, external, jacketed cooling with water, steam or thermal oil is usually not sufficient, due to the low heat transfer coefficient and area. Therefore, internal cooling has been employed to enhance heat extraction from the reactor, such as via water cooling [34]; while, it would be beneficial to generate steam directly from the internal cooling of the reactor, which, on the one hand, enhances the cooling effect by the two-phase heat transfer, and on the other hand, produces steam for the SOE, thus increasing overall heat-integration and efficiency.

2.2. Power-to-methane concept

The power-to-methane system investigated in this paper is illustrated in Fig. 1, following our previous discussion in [26]. The concept considers both SE (for comparison purpose) and CE to prepare the feedstocks for downstream methanation subsystem. For SE, CO_2 (18) is fed to the methane synthesis part, while for CE it is directly fed to the SOE via (20–21–22) by mixing with the fed steam (3) and recirculated gas (10). In such a case, the flow rates of CO_2 (20) and steam (1) can be adjusted together with other stack operating variables to obtain a gas composition (12) suitable for downstream synthesis [9].

For the methane synthesis and upgrading subsystem, hydrogen-rich gas mixture (23) is usually heated up to around 240 °C (25), depending on the catalysts employed, to start the methanation reactions. For SE, H_2 (12) and CO_2 (19) are fed stoichiometrically ($Z_{\text{H}_2}/Z_{\text{CO}_2} = 4$) for CO_2 methanation. For CE, the syngas composition (12) is recommended to achieve a molar-fraction based ratio $(Z_{\text{H}_2} - Z_{\text{CO}_2})/(Z_{\text{CO}} + Z_{\text{CO}_2})$ of around 3 [40]. The product (26, a gas mixture of H_2 , CO , CO_2 , CH_4 and H_2O) is then cooled down under the process pressure (4–30 bar) with water knock-out, before entering an upgrading module to obtain

desired methane purity (e.g., 98 vol.% for transportation fuel and 96 vol.% for gas-grid injection). Membrane-based upgrading module is preferred for compact system designs, because of commercial polymer membranes.

3. Process modeling

3.1. Solid-oxide electrolyzer

3.1.1. Consideration and assumption

A mathematical stack model is established and calibrated with experimental data to reasonably predict the performance for the conditions different from the experimental. The stack model is expected, as illustrated in Fig. 2, to cope with a wide range of input conditions (feed conditions (temperature, pressure, flow rate and composition), operating current density (reactant utilization factor, UF) and operating mode (isothermal or adiabatic)) to provide (a) the outlet conditions, (b) overpotential distribution, and (c) power consumption as well as heat exchanged (for isothermal operation). The resulting design/operating points will be further evaluated with practical constraints. The computational time for a single simulation should be kept as short as possible at the level of milliseconds to be capable of handling a number of iterations to reach specific design specifications/targets.

To meet the aforementioned requirements, the stack model should not be as complex as 3D or micro-structure models to reduce computational time, or as simple as lumped or 1D models to decrease the risk of wrong predictions for the conditions different from the experimental. Therefore, a quasi-2D (1D + 1D) cell model (as illustrated in Fig. 3) has been developed considering detailed electrochemistry, mass diffusion, chemical-reaction kinetics (and/or chemical equilibrium) and inter-connect resistances. The cell is discrete along the flow (X) direction, while both the cathode and anode are discrete vertically. Critical assumptions are made as follows:

- Mass diffusion between gas channels and the triple-phase boundary (TPB), where electrochemical reactions occur, happens only in a vertical manner.
- Heat transfer between segments is not calculated in detail but with a simple energy balance of each segment. There is no temperature gradient in the Y direction.
- Chemical equilibrium calculation, if applied, is performed only in gas channels, to avoid heavy computation if employed to each segment of the electrodes.
- Reaction kinetics for water–gas shift and methane–steam reforming are employed for each cathode segment.
- The current is attributed to H_2O and CO_2 splitting following the physical rule that there is only one common voltage for each

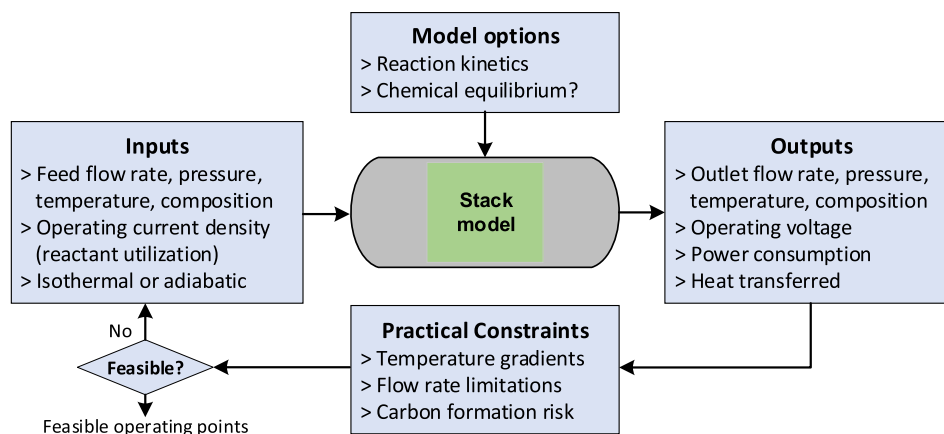


Fig. 2. Model inputs and outputs with critical operating constraints.

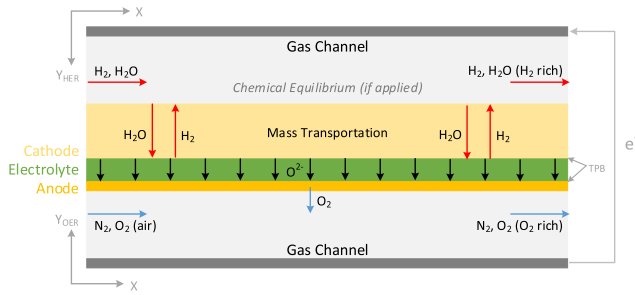


Fig. 3. Quasi-2D model developed for the solid-oxide cell (adapted from [26]) and a stack model can be aggregated by multiple cells plus the corresponding interconnects between cells.

segment.

In the literature, the attribution of current in CE is controversial: (1) Some believe that CO₂ electrolysis can play an important role in CE, for which the current is attributed via the concentration of H₂O and CO₂ at the TPB, e.g., [41–43]. (2) Some believe that CE is dominated by H₂O electrolysis [44], since the electrochemical performances observed were not affected by the feed compositions given a constant reactant content [45]. In the model improved in this paper, the attribution of current is not specified in subjective ways but calculated to ensure the voltage for H₂O splitting and CO₂ splitting are the same for each segment.

3.1.2. Governing equations

Most of the modeling equations employed below are based on the methodology developed by the group of Kee and Coltrin, e.g., [46], and its further improvements by, e.g., [43,47].

3.1.2.1. Mass transfer. The dusty-gas model (DGM) is employed to better describe multi-component gas transport within porous electrodes. The molar fraction of species i (H₂, H₂O, CO, CO₂, CH₄ and N₂ for the cathode, O₂ and N₂ for the anode) can be calculated by solving Eq. (4) [48,49]:

$$R T_K \left(\frac{\dot{N}_i}{D_{Kn,i}^{eff}} + \sum_{j=1}^n \frac{Z_j \dot{N}_i - Z_i \dot{N}_j}{D_{ij}^{eff}} \right) = - \left(p \nabla Z_i + Z_i \nabla p + Z_i \frac{B p}{D_{Kn,i}^{eff} \mu} \nabla p \right), \quad (4)$$

where R is the universal gas constant (J/mol/K), T_K is the absolute bulk gas temperature (K), \dot{N} is the molar flux (mol/s/m²), Z is the molar fraction (-), p is the total gas pressure (Pa), n is the number of species considered, and μ is the viscosity coefficient (Pa s). The permeability B (m²) can be evaluated by the Kozeny-Carmen equation [50] assuming that the electrodes are closely packed by spherical particles with a diameter d_p (m):

$$B = \frac{\epsilon^3 d_p^2}{72 \tau (1 - \epsilon)^2}, \quad (5)$$

with the ϵ and τ representing the porosity (-) and tortuosity (-) of the electrodes. The effective Knudsen diffusion coefficient ($D_{Kn,i}^{eff}$, m²/s) of the species i is formulated as

$$D_{Kn,i}^{eff} = \frac{\epsilon}{\tau} \frac{2 r_g}{3} \sqrt{\frac{8 R T_K}{\pi M_i}}, \quad (6)$$

where r_g is the pore radius (m) and M_i is the molecular weight (g/kmol) of the species i . The effective binary diffusion coefficient (D_{ij}^{eff} , m²/s) of the species i and j can be calculated as follows:

$$D_{ij}^{eff} = D_{j,i}^{eff} = \frac{\epsilon}{\tau} \frac{0.0026 T_K^{1.5}}{p \sqrt{\bar{M}_{ij} \sigma_{ij}^2 \Omega_D}}, \quad (7)$$

with the average molecular weight \bar{M}_{ij} and mean characteristic length σ_{ij} of a binary mixture (formed by species i and j) calculated by

$$\bar{M}_{ij} = \frac{2 M_i M_j}{M_i + M_j}, \quad (8)$$

$$\sigma_{ij} = (\sigma_i + \sigma_j)/2, \quad (9)$$

the dimensionless diffusion collision integral Ω_D evaluated by

$$\Omega_D = \frac{1.06036}{\left(\frac{k T_K}{\epsilon_{ij}}\right)^{0.1561}} + \frac{0.193}{e^{0.47635 \frac{k T_K}{\epsilon_{ij}}}} + \frac{1.03587}{e^{1.52996 \frac{k T_K}{\epsilon_{ij}}}} + \frac{1.76474}{3.89411 \frac{k T_K}{\epsilon_{ij}}}, \quad (10)$$

and average Lennard-Jones characteristic length ϵ_{ij} given as

$$\epsilon_{ij} = \sqrt{\epsilon_i \epsilon_j}. \quad (11)$$

The values of the characteristic lengths σ_i and ϵ_i of each species involved are listed in Table A.1.

The molar flux of each species at each segment should be given to solve Eq. (4). At the TPB, where the electrochemical reactions occur, the molar flux of each species i is given as

$$\dot{N}_i^{her,TPB} = + \frac{1 e 4 J_i}{2 F}, \quad i = \text{H}_2\text{O}, \text{CO}_2, \quad (12)$$

$$\dot{N}_i^{her,TPB} = - \frac{1 e 4 J_i}{2 F}, \quad i = \text{H}_2, \text{CO}, \quad (13)$$

$$\dot{N}_{\text{O}_2}^{oer,TPB} = - \frac{1 e 4 J_{\text{O}_2}}{4 F}, \quad (14)$$

where J_i is the current density (always taken as positive here, A/cm²) attributed to the active species i , and the positive and negative signs stand for the diffusion towards the TPB and the gas channels, respectively. Within the electrode, the molar flux originates from the chemical reactions:

$$\nabla \dot{N}_i^{her} = \dot{r}_i / 3.6, \quad (15)$$

$$\nabla \dot{N}_i^{oer} = 0, \quad (16)$$

where the \dot{r}_i is the reacting rate (kmol/h/m³) of the species i considering all chemical reactions.

For the gas channel, the mass transfer is described by considering the interaction with the mass diffusion within the electrodes:

$$\nabla \dot{F}_i^{her} = -3.6 \omega \dot{N}_i^{her,0} + \sum_{i_{rxn}} c_{i_{rxn},i} \dot{n}_{eq,i_{rxn}}, \quad (17)$$

$$\nabla \dot{F}_i^{oer} = -3.6 \omega \dot{N}_i^{oer,0}, \quad (18)$$

where $\dot{n}_{eq,i_{rxn}}$ is the extent (kmol/h) of the reaction i_{rxn} due to chemical equilibrium at the gas channel, $c_{i_{rxn},i}$ is the stoichiometry coefficient (-) of the species i for the reaction i_{rxn} and ω is the width of the electrode (m).

3.1.2.2. Heat transfer. The temperature is uniformly distributed along Y-direction. The energy balance is formulated as

$$\nabla \dot{E}_{her,gc} + \nabla \dot{E}_{oer,gc} + \nabla \dot{E}_{elec} + \nabla \dot{Q}_{loss} = 0, \quad (19)$$

where $\dot{E}_{her} = \dot{F}_{her} h_{her}$ and $\dot{E}_{oer} = \dot{F}_{oer} h_{oer}$ are the total enthalpy (including the enthalpy of formation) of the bulk in the gas channels, with \dot{F} and h for molar flowrate (kmol/h) and molar specific enthalpy (GJ/kmol). The \dot{E}_{elec} and \dot{Q}_{loss} are the electricity consumed and heat losses to the environment, respectively.

3.1.2.3. Chemical reaction. Chemical equilibrium in the gas channel can be calculated to obtain the reaction extents and equilibrium compositions. The kinetics of the reactions occurring in the electrode (WGS and steam-methane reforming reaction (SMRR)) are taken from solid-oxide fuel cell [51–53] with the reaction rates \dot{r} (kmol/h/m³)

expressed as follows:

$$\dot{r}_{\text{SMRR}} = 0.053e^{-\frac{82000}{R} \left(\frac{1}{T_K} - \frac{1}{873} \right)} Z_{\text{CH}_4} \frac{3.6}{\delta_{\text{her}}}, \quad (20)$$

and

$$\dot{r}_{\text{WGSr}} = \frac{Z_{\text{CO}} Z_{\text{H}_2\text{O}} - Z_{\text{CO}_2} Z_{\text{H}_2}}{e^{39258 - 40.555 T_K + 0.004375 T_K^2} \omega \delta_{\text{her}} L},$$

with the ω , δ , and L are the width (m), thickness (m) and length (m) of the electrode.

With the calculated reaction rates, the rate (kmol/h/m³) of each species can be obtained by

$$\dot{r}_i = c_{\text{SMRR},i} \dot{r}_{\text{SMRR}} + c_{\text{WGSr},i} \dot{r}_{\text{WGSr}} \quad (21)$$

3.1.2.4. Electrochemistry. The electrochemistry is expressed for each electrochemically-active species (H₂ and CO):

$$V_i = V_{\text{Nernst},i} + V_{\text{act},i}^{\text{her}}(J_i) + V_{\text{act},i}^{\text{over}}(J_i) + V_{\text{ohm},i}(J_i) + V_{\text{mic},i}(J_i), \quad i = \text{H}_2, \text{CO} \quad (22)$$

where the Nernst potential (V_{Nernst}) and overpotentials due to the activation of electrochemical reaction (V_{act}), ohmic resistance (V_{ohm}) and interconnect (V_{mic} , if applied), can be calculated as follows:

– Nernst potential including the concentration overpotential (the \ln term)

$$V_{\text{Nernst},\text{H}_2} = (-2.87902 \text{ e} - 4 T_C + 1.20672) + \frac{R T_K}{2F} \ln \left(\frac{Z_{\text{H}_2}^{\text{her,TPB}} \sqrt{p_{\text{tot}}^{\text{over}} Z_{\text{O}_2}^{\text{over,TPB}}}}{Z_{\text{H}_2\text{O}}^{\text{her,TPB}}} \right), \quad (23)$$

$$V_{\text{Nernst},\text{CO}} = (-4.50090 \text{ e} - 4 T_C + 1.34110) + \frac{R T_K}{2F} \ln \left(\frac{Z_{\text{CO}}^{\text{her,TPB}} \sqrt{p_{\text{tot}}^{\text{over}} Z_{\text{O}_2}^{\text{over,TPB}}}}{Z_{\text{CO}_2}^{\text{her,TPB}}} \right), \quad (24)$$

where Z_i^{TPB} is the molar fraction of the species i at the TPB, p_{tot} is the total pressure (bar) and F is the Faraday constant (9.6485e4 C/mol).

– Activation overpotential following Butler-Volmer equation employed in [43]

$$J_{\text{H}_2} = J_{0,\text{H}_2} \left(e^{\frac{F(1+\beta_{\text{H}_2}^{\text{over}})V_{\text{act},\text{H}_2}^{\text{her}}}{R T_K}} - e^{-\frac{F\beta_{\text{H}_2}^{\text{her}}V_{\text{act},\text{H}_2}^{\text{her}}}{R T_K}} \right), \quad (25)$$

$$J_{\text{H}_2} = J_{\text{O}_2}^{\text{H}_2\text{O}-\text{H}_2} = J_{0,\text{O}_2} \left(e^{\frac{F\beta_{\text{H}_2}^{\text{over}}V_{\text{act},\text{H}_2}^{\text{her}}}{R T_K}} - e^{-\frac{F\beta_{\text{H}_2}^{\text{her}}V_{\text{act},\text{H}_2}^{\text{her}}}{R T_K}} \right), \quad (26)$$

$$J_{\text{CO}} = J_{0,\text{CO}} \left(e^{\frac{F\beta_{\text{CO}}^{\text{over}}V_{\text{act},\text{CO}}^{\text{her}}}{R T_K}} - e^{-\frac{F(1+\beta_{\text{CO}}^{\text{her}})V_{\text{act},\text{CO}}^{\text{her}}}{R T_K}} \right), \quad (27)$$

$$J_{\text{CO}} = J_{\text{O}_2}^{\text{CO}_2-\text{CO}} = J_{0,\text{O}_2} \left(e^{\frac{F\beta_{\text{CO}}^{\text{over}}V_{\text{act},\text{CO}}^{\text{her}}}{R T_K}} - e^{-\frac{F\beta_{\text{CO}}^{\text{her}}V_{\text{act},\text{CO}}^{\text{her}}}{R T_K}} \right), \quad (28)$$

where J_0 is the exchange current density (A/cm²) and β is the asymmetry charge-transfer co-efficient of the electrodes (–). The exchange current density for the electrochemical reactions can be calculated by the saturation exchange current density (J^* , A/cm²) and saturation pressure (p^* , bar) at the TPB:

$$J_{0,\text{H}_2} = J_{\text{H}_2}^* \frac{(p_{\text{H}_2}^{\text{her,TPB}}/p_{\text{H}_2}^*)^{0.25} (p_{\text{H}_2\text{O}}^{\text{her,TPB}})^{0.75}}{1 + \sqrt{p_{\text{H}_2}^{\text{her,TPB}}/p_{\text{H}_2}^*}}, \quad (29)$$

$$J_{0,\text{CO}} = J_{\text{CO}}^* \frac{(p_{\text{CO}_2}^{\text{her,TPB}}/p_{\text{CO}}^*)^{0.25}}{1 + \sqrt{p_{\text{CO}}^{\text{her,TPB}}/p_{\text{CO}}^* + p_{\text{CO}}^{\text{her,TPB}}/p_{\text{CO}_2}^*}}, \quad (30)$$

$$J_{0,\text{O}_2} = J_{\text{O}_2}^* \frac{(p_{\text{O}_2}^{\text{her,TPB}}/p_{\text{O}_2}^*)^{0.25}}{1 + \sqrt{p_{\text{O}_2}^{\text{her,TPB}}/p_{\text{O}_2}^*}}, \quad (31)$$

with the J^* and p^* given by [43,46,47,54]:

$$J_i^* = k_i e^{-\frac{E_{\text{act},i}}{R T_K}}, \quad i = \text{H}_2, \text{CO}, \text{O}_2, \quad (32)$$

where the k and E_{act} are the pre-exponential factor (A/cm²) and activation energy (J/mol), given in Table A.2, and

$$p_i^* = \frac{\Gamma_i}{\gamma_i} \sqrt{2\pi R T_K M_i} k_{d,i} e^{-\frac{E_{d,i}}{R T_K}}, \quad i = \text{CO}_2, \text{CO}, \text{H}_2, \quad (33)$$

$$p_{\text{O}_2}^* = k_{d,\text{O}_2} e^{-\frac{E_{d,\text{O}_2}}{R T_K}}. \quad (34)$$

where Γ is the surface site density (mol/m²), γ is the sticking coefficient (–), k_d and E_d are the pre-exponential factor (1/s) and activation energy (J/mol) of the desorption. The values of the parameters involved in these equations are listed in Table A.3.

– Ohmic overpotential due to the electrolyte

$$J_i = \frac{V_{\text{ohm},i}}{\delta_e} \left(\frac{k_e}{T_K} e^{-\frac{E_e}{R T_K}} \right) \quad (35)$$

where k_e and E_e are the pre-exponential factor (S K/m) and activation energy (J/mol) of the Arrhenius expression for the electrolyte, and δ_e is the thickness (m) of the electrolyte. The values of the parameters are given in Table A.4.

– Overpotential related to interconnect

$$J_i = \frac{V_{\text{mic},i}}{\delta_m} \left(\frac{k_m}{T_K} e^{-\frac{E_m}{R T_K}} \right) \quad (36)$$

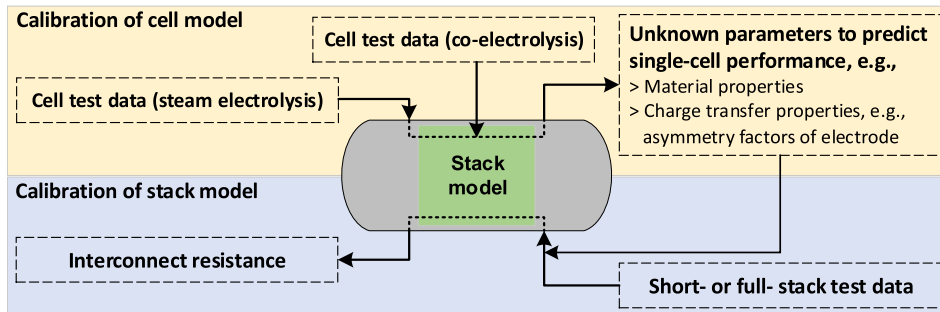


Fig. 4. Calibration procedure: from the cell to stack level.

where k_{mic} and E_{mic} are the pre-exponential factor (S K/m) and activation energy (J/mol) of the Arrhenius expression for the interconnect, and δ_{mic} is the thickness (m) of the interconnect. The formulation is similar to Eq. (35) but only exists at the stack level to represent the performance difference between the cell and stack tests. The values of the parameters are also given in Table A.4.

The attribution of current density for H_2O and CO_2 splitting follows the physical fact that there is only one voltage for each cell. Therefore, this voltage-based attribution can be determined by satisfying the Eq. (37) to each segment:

$$V_{\text{CO}}(J_{\text{CO}}) = V_{\text{H}_2}(J_{\text{H}_2}). \quad (37)$$

3.1.3. Calibration procedure

The resistance of a stack is contributed mainly by the serial repeating unit (SRU, including cell, interconnect and others). It is recommended to estimate unknown or uncertain parameters based on consistent experimental test data from cell to stack with both SE and CE. It is also recommended to follow the procedure given in Fig. 4:

- Step 1: The test data of single-cell SE are employed to calibrate the unknown or unmeasured parameters related to SE, e.g., material properties for charge transfer or asymmetry factors of the Butler-Volmer equation.
- Step 2: The test data of single-cell CE are then applied together with the estimated parameters from step 1 to estimate those parameters related to CO_2 electrolysis.
- Step 3: With the estimated parameters in step 1 and 2, the stack test data for both steam and CE are employed to calibrate other resistances, particularly, of the interconnect.

With this procedure, the performance difference between stack and cell is attributed to the interconnect, which is rather ideal in practice, since the stack performance is affected by many additional factors, e.g., flow distribution, sealing effectiveness, etc. In addition, single cell tests sometimes are conducted with button cells, which may perform differently from the cells with a larger footprint for the stack. Also, it is recommended to employ the data from different test conditions.

3.1.4. Self-adaptive stack model for downstream synthesis processes

The stack model developed above might not be suitable to simulate the power-to-fuel systems, since it cannot readily find suitable operating points considering downstream synthesis processes and various design specifications. The controllable variables of the hot box (the SOE subsystem) are cathode recirculation ratio, current density (voltage), CO_2 feed flow rate (for CE), and steam and sweep-gas feed flow rates, which determine, respectively and interactively, the four design specifications: inlet H_2 content (usually 10 vol.% [55,56]), reactant utilization, syngas modular number ($(Z_{\text{H}_2} - Z_{\text{CO}_2})/(Z_{\text{CO}} + Z_{\text{CO}_2})$ of the dry product (for CE only, around 2 for methanolization and 3 for methanation), and the temperature gradient (usually maximum 120 °C between the stack inlet and outlet). It becomes difficult to manually adjust these variables to satisfy simultaneously these design specifications, e.g., the expected reactant utilization with suitable syngas for methanation. Therefore, a self-adaptive procedure is proposed in Fig. 5 with nested iteration loops. Given the inlet parameters, several controllable variables can be iteratively adjusted to target the expected design specifications. The obtained operating points can be further evaluated with other practical constraints, e.g., flow limitation, carbon formation risk, to find potential operating points.

3.2. Other components

The modeling of most of the remaining components have been introduced and discussed in detail in [26] with a summary given below:

- **Methanation reactor:** The model employed does not consider reaction kinetics but is simply based on chemical equilibrium (Requil model in Aspen Plus). The fixed-bed reactor operating isothermally at 290 °C (the optimal operating temperature for several commercial catalysts as identified in [16]) is employed with the outlet gas reaching chemical equilibrium. Leveling reactor temperature at 290 °C might be achieved by the internal steam generation when the two-phase heat transfer occurs in the reaction zone. The effects of operating conditions and gas compositions on the conversion rate and outlet gas compositions have been discussed in detail in [26] and will not be repeated here.
- **Membrane module:** A 1D model applicable for counter-, co- or cross-flow configurations is employed with all detailed equations given in [26]. Considering the cost, selectivity and permeability among various membranes of organic polymers and non-organic materials, the polyimide membrane is employed with the permeability (Barrer) at 30 °C reported as H_2 28.1, N_2 0.32, O_2 2.13, CH_4 0.25, CO_2 10.7 [57], and therefore high selectivity: H_2/CH_4 112.4 and CO_2/CH_4 42.8.
- **Gas compressors:** Multi-stage adiabatic compressors with inter-stage cooling and isentropic compression are considered and modeled by the MCompr model in Aspen Plus. The number of stages is determined by a maximum pressure ratio of 4 and equal pressure ratio among all stages. The isentropic efficiency of each stage 75%. The inter-stage cooling temperature is set at 40 °C. Although isothermal compression requires significantly less work than adiabatic compression for high final pressure (MPa level) [58], adiabatic compression considered here will not introduce a big difference in the system performance indicators, since the major power consumption of power-to-fuel systems comes from electrolysis and electrical heating (if used).
- **DC/AC inverter:** The loss of DC/AC converter is not considered. Introducing inverter losses only reduces all efficiency number proportionally. However, in the supporting information, along with the discussion in Section 5, the effect of inverter loss (5–10%) is illustrated but is not discussed in detail.
- **Heat exchanger network:** The heat exchangers are not calculated

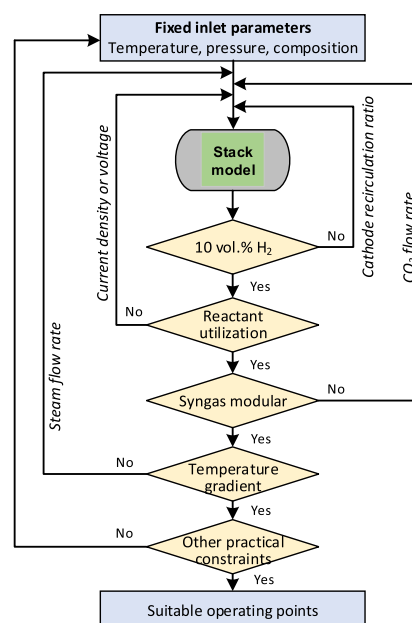


Fig. 5. Self-adaptive procedure to reach design specifications (in the yellow diamonds) by changing the controllable variables (italic). The design specification of syngas modular is not active for SE without CO_2 flow fed into the electrolyzer. (For interpretation of the references to colour in this figure legend, the reader is referred to the web version of this article.)

in detail but is estimated by the classical heat cascade calculation with predefined minimum temperature differences of each heat flow. The losses of heat exchangers are not considered, since the heat losses depend on the component design and insulation, and can hardly be estimated reasonably. However, in the [supporting information](#), along with the discussion in Section 5, the effects of heat losses (2–5% for the stack, 10% for heat transfer from current industrial practice) are illustrated but not discussed in detail.

- **Hot and cold utilities:** Only electrical heating is used as the hot utility and cooling water from the river or lake as the cold utility. The energy efficiency of electrical resistance heating is assumed as 100%. The cooling water is assumed unlimited at 20 °C.

4. Methodology and specifications for conceptual system design

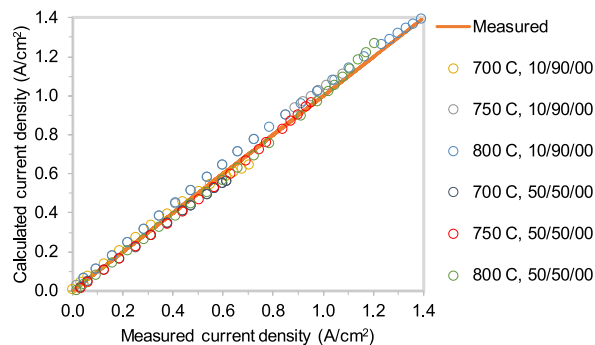
The effects of design variables on the process design should be investigated not with a specific system layout but at the level of conceptual design, since the improvement of system performance is usually contributed the most by changing the system layout [59]. Thus, in this study, the system layout is freed without defining a specific heat exchanger network (HEN), whose performance will be estimated via classical chemical engineering approach described elsewhere, e.g., [39]. For the considered system, it has been proven in [19] that the system with specifically-designed HEN can perform closely to the corresponding conceptual design, which emphasizes the rationality of such parametric investigation. However, the conceptual design with variable system layouts can be difficult to be handled due to the combinatorial nature of integer variables (particularly involved in the heat-cascade calculation) and high nonlinearity involved [59], which easily lead the mathematical problem to a large-scale, difficult-to-solve mixed-integer nonlinear programming (MINLP) problem. Thus, decomposition methods are usually employed to cope with the integrity and nonlinearity separately in two levels by hybrid algorithms.

In this paper, an in-house bi-level optimization platform, OSMOSE, was employed in a similar fashion as [26]. The upper-level algorithm generates new designs with a set of new operating/design variables, which will be specified to the aspen models employed. After solving the nonlinear aspen models, the simulation results (e.g., mass flowrates of material flows, temperatures and loads of heat flows) are structured as the inputs for the lower-level mixed-integer linear programming (MILP) problem to minimize the hot and cold utilities needed to close the energy balance. Afterwards, the objective functions of each conceptual design with specific operating/design points of the involved components are calculated and piped back to the upper-level algorithm to decide whether to keep or discard the evaluated designs.

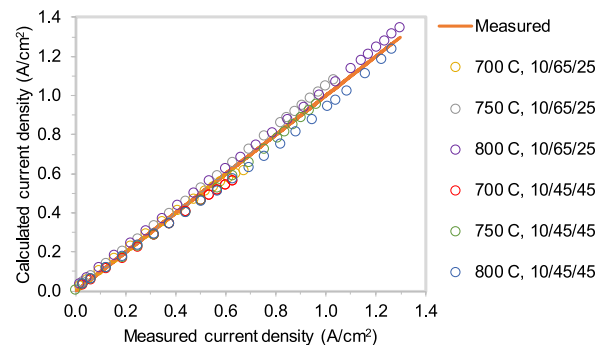
The optimization problem to be investigated is defined by two objective functions, i.e., the overall system efficiency and methane production (the flowrate of the stream 32 in Fig. 1), and five key design variables. The system efficiency is defined as the ratio of energy (based on either HHV or lower heating value (LHV)) stored in the methane produced and the total power consumed by all system components including the SOE, the compressors, fans and pumps, and electrical heater, which is used as the only hot utility to close energy balance of the whole system. The decision variables and their bounds considered are

- for the SOE, operating pressure (1.1–30 bar), electrochemical utilization factor (50–80%), steam flowrate (2.5–25 sccm/cm²) and sweep-air feed flowrate (0–40 sccm/cm²),
- for the methanator, operating pressure (1.1–30 bar), and
- for the membrane module, permeate pressure (0.5–15 bar).

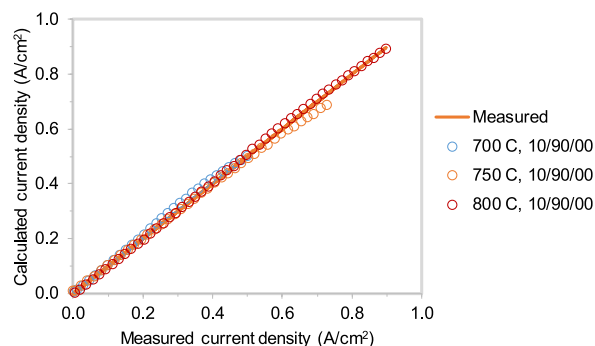
If the sweep-air feed becomes zero, then the SOE will be operated with pure oxygen production. The fixed parameters are a stack inlet temperature (700 °C), a maximum temperature difference between the stack inlet and outlet (120 °C), a methanation temperature (290 °C), a



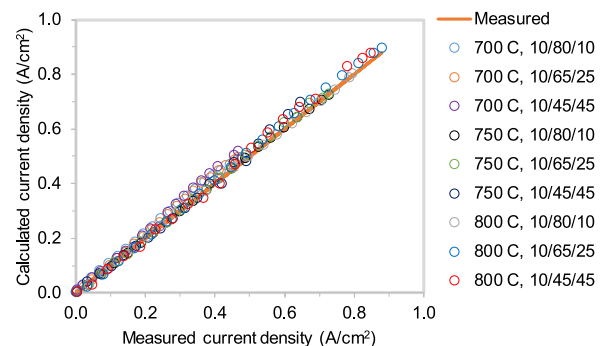
(a) For single cell SE (J-V curves given in Fig. S3)



(b) For single cell CE (J-V curves given Fig. S4)



(c) For SRU SE (J-V curves given Fig. S5)



(d) For SRU CE (J-V curves given Fig. S6)

Fig. 6. Parity plots to show the agreement between prediction and measurement.

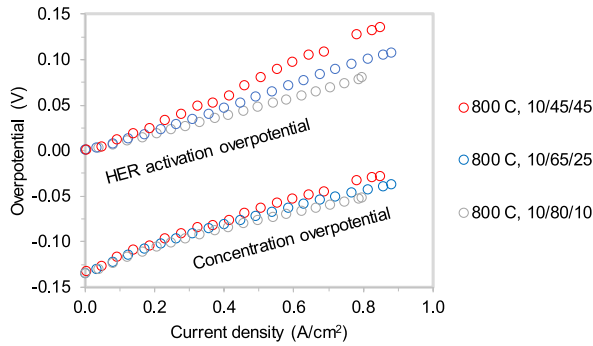


Fig. 7. The effect of CO₂ feed fraction on concentration and activation overpotentials of H₂O splitting at 800 °C and 1 bar with the feed molar composition given in H₂/H₂O/CO₂ (vol.%).

gas-grid pressure (85 bar), and syngas compositions (for CE only) with a module number $(Z_{H_2} - Z_{CO_2})/(Z_{CO} + Z_{CO_2})$ of 3.1.

5. Results and discussion

5.1. SOE model calibration

The cell and stack tested were provided by a leading manufacturer in Europe. The structure of the fuel-electrode supported cells (with an active area of 80 cm²) is a thin 8 mol.% (YSZ) electrolyte (ca 10 μm), a porous Ni/YSZ fuel electrode (ca. 250 μm), a (La,Sr)(Co,Fe) O_{3-δ} (LSCF) perovskite based oxygen electrode, and a Gd₂O₃-doped CeO₂ barrier layer applied on the electrolyte. The cells can be stacked with ferritic stainless-steel interconnect coated with a MnCo₂O₄ protective layer. The tests were performed by Technical University of Denmark within the scope of ECo [12] for a single cell and Technical Research Center of Finland within the scope of SOPHIA [60] for a 6-cell SOE short stack [61]. The single cell was tested at 700/750/800 °C and 1 bar with the anode swept by an oxygen flow of 145 sccm/cm² and a cathode feed of 12 sccm/cm². The reactant feed compositions (H₂/H₂O/CO₂, vol.%) are 10/90/00 and 50/50/00 respectively for the SE tests, and 10/65/25 and 10/45/45 for the CE tests. The J-V curves obtained are given in Fig. S1. The stack was tested at 700/750/800 °C and 1 bar with the anode swept by an air flow of 51.4 sccm/cm² and a cathode feed of 12 sccm/cm². The reactant feed compositions (H₂/H₂O/CO₂, vol.%) are 10/90/00 for the SE tests, and 10/80/10, 10/65/25 and 10/45/45 for the CE tests. The J-V curves for the average SRU performance obtained are given in Fig. S2. It is considered that the employed experimental performances are consistent enough to distinguish the cell and SRU.

To use these test experimental data, the model described in Section

3.1.2 was reformulated in a mathematically-sound way in Aspen Custom Modeller, as given in Part B of the supporting information. The parameters to be estimated as listed in Tables A.1 and A.4 include the pre-exponential factors and activation energy related to exchange current densities (Eq. (32)), the asymmetry factors used for activation overpotentials (Eqs. (25)–(28)) and the parameters related to the resistance of interconnect (Eq. (36)). The parameter estimation was performed with the geometry parameters given in Table A.5 and other fixed parameters listed in Tables A.1–A.4 (if references are given). The estimated values of the chosen parameters are also listed in Tables A.3 and A.4.

The parity plots are used to show the prediction accuracy as shown in Fig. 6: The closer the scattered points to the reference line, the higher the accuracy will be. Thus, good agreement has been reached for all experimental and prediction points under all considered conditions. It is also observed from Figs. S3–S6 that, for the tests at 700 °C and relatively large current density, the prediction accuracy reduces but remains at a high level. For such conditions, the predicted voltage is slightly higher than the measured value, which indicates that the reactant starvation may occur at a current density lower than the reality. Nevertheless, it can be concluded that the calibrated model is satisfactory for the purposes of this paper and the average SRU performance can be aggregated to represent the stack performance.

5.2. Role of CO₂ in co-electrolysis

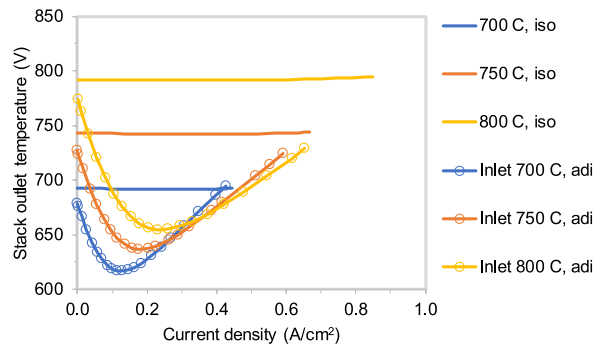
The attribution of current density to H₂O and CO₂ electrolysis used in literature is often concentration-based rather than voltage-based as proposed in Section 3.1.1. To investigate the role of CO₂ during CE, a factor (ϕ) is defined for each segment to indicate how the obtained current attribution deviates away from the concentration ratio:

$$\phi = \frac{J_{H_2O}}{J_{H_2O} + J_{CO_2}} \frac{Z_{H_2O}^{TPB} + Z_{H_2O}^{TPB}}{Z_{H_2O}^{TPB}}, \quad (38)$$

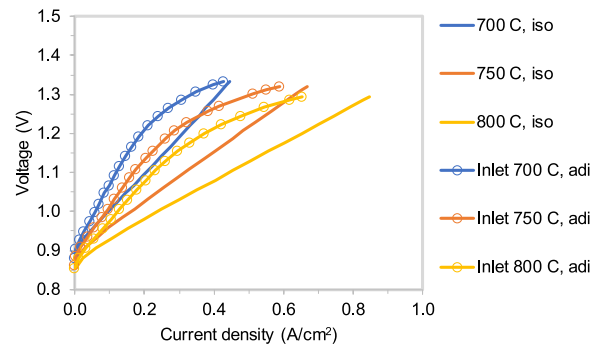
where Z_i^{TPB} is the molar fraction of the species i at the TPB. The average factor over all segments, $\bar{\phi}$, can thus be used to evaluate the current attribution of a specific operating point: (1) The closer the $\bar{\phi}$ to one, the more confident the current attribution is concentration-based; (2) the larger the $\bar{\phi}$ below one, the more dominated the current attribution to CO₂ will be; and (3) the larger the $\bar{\phi}$ above one, the more dominated the current attribution to H₂O will be.

The $\bar{\phi}$ profiles versus applied current density for the CE are given in Fig. S7. It shows that (1) the factor is over one for all points, and (2) the higher the CO₂ feed fraction, the larger the factor will be. Therefore, the electrochemical splitting of co-electrolysis is dominated by H₂O splitting, while the CO₂ is converted by RWGSR.

It is also observed from Fig. S2(b) that, at the same temperature, the operating voltage rises with an increase in the feed CO₂ fraction. It is



(a) Stack outlet temperature versus current density



(b) SRU J-V curves

Fig. 8. Comparison of predicted isothermal (iso) and adiabatic (adi) performances of CE with a reactant feed of 12 sccm/cm² (10/65/25 vol.% H₂/H₂O/CO₂) and no sweep gas.

found that the thermodynamic potential (temperature-dependent part of the Nernst potential (Eq. (23)), the OER activation overpotential and the total ohmic overpotential are affected very limited by CO_2 concentration (Fig. S8); however, both the overpotentials of concentration and HER activation increase largely with an increased CO_2 fraction (Fig. 7), due to the decrease in partial pressure of H_2O locally at the TPB.

5.3. Isothermal vs adiabatic operation

Practical (quasi-adiabatic) stack performance differs from the experimental (quasi-isothermal), whose temperature is stabilized by electrical heating considering internal heat release and large heat losses (experimental setups are usually not well insulated). There are limited temperature variations during experiments (below, e.g., 10°C); however, under adiabatic conditions, the electrochemical performance and stack temperature strongly interact as exemplarily shown in Fig. 8(a) for CE: For given feed conditions, an increase in the current density leads to V-shaped profiles of the stack outlet temperature. When applying no or small current density, the outlet temperature drops due to the endothermic RWGSR for CO_2 conversion. Along with the increase in current density, the internal heat losses due to overpotentials are increased, thus compensating heat absorbed by the RWGSR and further elevating the outlet temperature. The temperature variation can be reduced by increasing sweep-gas feed, which can supply heat to maintain stack temperature or extract heat to cool down the stack. For the cases in Fig. 8(a) without sweep gas, the local temperature can be 150°C less than the inlet temperature under adiabatic operation and can become even lower considering heat losses in practical applications. As a consequence, the electrochemical performance in practice might be worse than the experimental (Fig. 8(b)). It is also indicated in Fig. 8 that high current density might be preferred in practice.

Regarding these observations, the use of experimental cell/stack results (e.g., area specific resistance at a certain temperature) might lead to an overestimation of stack and system performances. Therefore, the procedure described in Section 3.1.4 is recommended to identify feasible (realistic) stack operating points for system-performance prediction.

5.4. Understanding pressurized operation and internal methanation

5.4.1. At the stack level: conditions to maximize internal methanation

Qualitatively speaking, in a closed reacting system, the exothermic methanation reaction (Eq. (1)) can be pushed toward methane production by reducing temperature and increasing pressure. However, since the stack is operated at over 600°C , the decrease in temperature is expected to contribute less than the increase in pressure. For internal methanation, an additional driving force is provided by the continuous removal of O_2 from the reacting mixture via electrolysis of H_2O , which consumes the product H_2O and generates the reactant H_2 , thus enhancing the driving force from the increased partial-pressure difference between the reactants and products. From the viewpoint of compound balance, the removal of O_2 leads the reacting mixture toward the

products with high H/C ratio, i.e., CH_4 in the presence of nickel under high pressure. The above fundamental insights, however, cannot tell quantitatively: (1) which are the most influential operating variables, and (2) how much fraction of methane can be achieved inside the stack.

To investigate these, two analyses have been made subsequently. The five operating variables (i.e., the pressure, current density, UF, inlet temperature, sweep-air flowrate) are varied first in a one-in-a-time scheme from the base point. The results in Fig. S9 show that varying a single variable cannot promote a very high internal methane production. The most influential variable is the operating pressure, which can bring the outlet methane fraction up to 8% (vol.% dry gas). The current density and the UF shows limited impacts. Varying solely the inlet temperature or sweep-air flowrate has a very limited contribution. However, what will be the maximum methane fraction if the variables are varied simultaneously?

The preferred conditions to maximize the outlet methane fraction are further investigated in Fig. 9. Starting from the base point, the four variables, pressure, UF, sweep-air feed and current density are subsequently investigated by keeping each favored value of each variable already investigated. The base operating point produces a very limited amount of methane under atmospheric pressure. By increasing the pressure up to 30 bar the methane fraction reaches 7% (vol.% dry gas). Due to the heat released by the methanation reaction, the stack outlet temperature increases dramatically from 720°C to 820°C . When keeping the pressure at 30 bar and increasing the UF from 50% to 80%, the methane production is further enhanced with its molar fraction reaching up to 14%. Consequently, the stack outlet temperature is further increased up to over 860°C . To control the stack temperature within the practical limit, the sweep-air feed is increased up to 30 sccm/ cm^2 leading to a drop of the stack operating temperature, which in turn increases the outlet methane fraction over 22% (vol.% dry gas). The stack temperature can also be further reduced by lowering the current density due to less internal heat losses by the reduced overpotential. The current density should not be too low for economic purpose. At $0.3\text{ A}/\text{cm}^2$, the outlet methane fraction can even reach close to 30% with the stack outlet temperature controlled close to the inlet temperature. Therefore, the preferred conditions to promote internal methanation are high pressure, UF and sweep-gas feed as well as small current density. Considering the variable ranges used in this section, the conditions to maximize internal methanation is identified as 30 bar, 80% UF, 30 sccm/ cm^2 sweep-air feed and $0.3\text{ A}/\text{cm}^2$ current density.

However, it is not clear whether such operating points with high internal methanation are favorable from the system viewpoint. Particularly, compressing air up to 30 bar will penalize the system efficiency. Therefore, the benefits of promoting internal methanation need to be identified at the level of the overall system.

5.4.2. At the system level: the effects of operating pressure and internal methanation

The conceptual system design is re-investigated and compared with our previous results [26]. The optimization methodology of both studies is the same as briefly described in Section 4, while the major difference comes from the employed SOE models. The first results

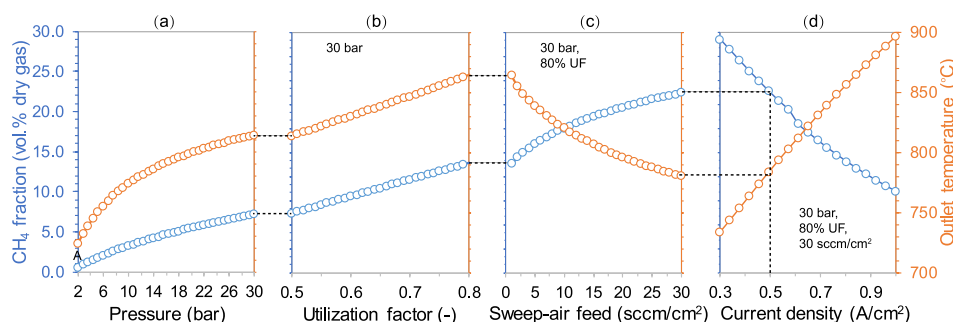
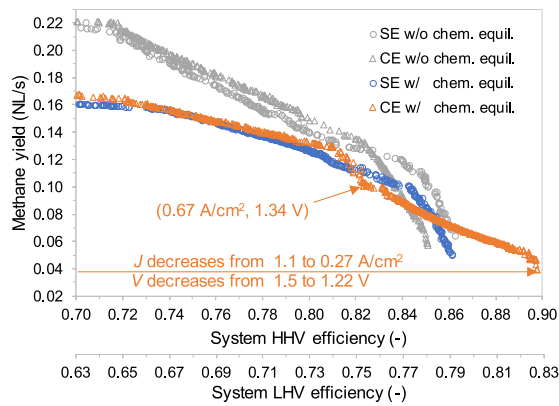
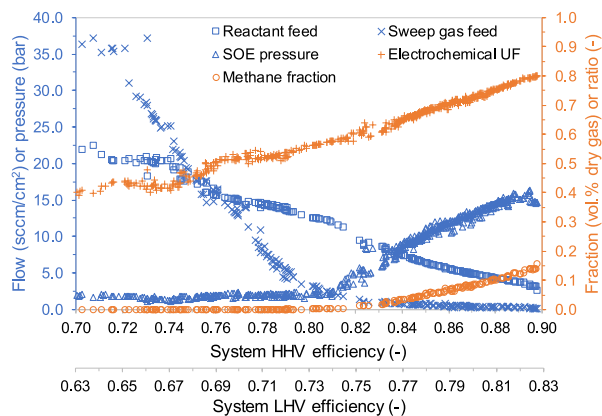


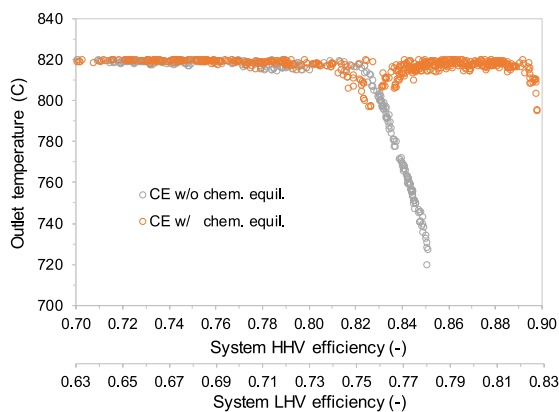
Fig. 9. The identification of the conditions to maximize the internal methanation. Starting from the base point (A) at 700°C (inlet temperature) and 1 bar with 1 sccm/ cm^2 sweep-air feed and 50% utilization factor, each variable is assigned successively with the preferred value from (a) to (d). Note that (1) the CO_2 feed flow is always adjusted to achieve a syngas module for downstream external methanation, (2) not all points in the figure are practically feasible considering the maximum-allowed temperature difference inside the stack, and (3) no heat losses are considered.



(a) Trade-off between methane yield and system efficiency.



(b) Variation of the key variables of the new CE solutions.



(c) Variation of the outlet temperature for both CE cases.

Fig. 10. System-level investigation on the pressurized operation and internal methanation with the optimization specifications given in Section 4. As a comparison, the calculations based on the old SOE model employed in [26] are also given (in gray). The methane yield is for a system with a stack of a total active area of 5120 cm². The figures presented here do not consider the AC/DC inverter losses and heat losses; however, the effects of these two type of losses are illustrated in Figs. S10 and S11. All these losses might cause a decrease in the system efficiency by up to 8 percentage points.

(Fig. 10(a)) obtained from the bi-objective optimization are the trade-off between methane yield and system efficiency, as comprehensively discussed in [26,59,62]: The increase in methane yield leads to a decrease in system efficiency. The major reasons are (1) the increase in current density to boost methane yield leads to an increased

overpotential, which reduces the electrolysis (electrical) efficiency and thus the system efficiency; and (2) to provide sufficient cooling for the stack operated with an increased current density, steam feed needs to be increased, which reduces reactant utilization and worsens system-level heat integration. It is also shown that, with the same system efficiency, the newly-obtained Pareto solutions mostly show less methane yield than the old. This is because of the difference between the electrochemical performances predicted by the two SOE models: With the new model, the predicted voltage is slightly higher than that of the old for the same current density, and the difference becomes larger at a high current density (e.g., over 1.0 A/cm²), which happens due to that all the employed experimental points are below 1.0 A/cm². Therefore, the difference of methane yield is large at the low efficiency part with large current densities but is reduced gradually with the increase in system efficiency (the decrease in current density). Nevertheless, all Pareto fronts show similar trade-offs and it is confident to discuss the design points with over 80% efficiency (with a relatively low current density below 0.8 A/cm²).

The main difference caused by introducing chemical equilibrium (or internal methanation) is illustrated by the Pareto solutions with efficiencies over 80% in Fig. 10(a). From the design point with 0.67 A/cm² and 1.34 V, the new Pareto front of CE case goes differently from the old: The efficiency range of the new CE front is extended, reaching up to 90%. The reasons are further investigated by the variations of the key variables in Fig. 10(b), which shows that, starting from around 80% efficiency (HHV), the pressurized operation is preferred and, together with a high UF, the internal methanation is promoted. The maximum methane fraction obtained is around 15 vol.% (dry gas) with the stack operated at 15 bar with 2.7 sccm/cm² steam feed, 80% UF (corresponding to 0.26 A/cm²) and no sweep gas. This point is quite far away from the favorable conditions identified at the stack level with a methane fraction (dry gas) of 30 vol.% (Section 5.4.1). Particularly, large sweep-gas feed for pressurized operation is not preferred to enhance system efficiency. The expected electrolysis pressure is not as high as 30 bar.

The remaining questions become (1) why the internal methanation becomes preferred starting from a relatively small current density/voltage (below 0.6 A/cm² at 700 °C (stack inlet temperature)) and (2) why the maximum amount of internal methanation expected is less from the system perspective? These are due to the interaction among electrochemistry (J-V variation in Fig. 10(a)), internal methanation (Fig. 10)) and stack temperature (Fig. 10(c)). When the voltage (overpotential) becomes not enough to maintain the stack temperature as high as possible to ensure the highest possible electrolysis efficiency, the strongly-exothermic methanation reaction will be promoted internally, which requires a pressurized operation. As shown in Fig. 10(c), the outlet temperature of the old CE case without internal methanation drops, since no other heat sources in the stack can compensate the reduced heat produced (due to the decreased overpotentials) so that the high stack temperature can be maintained; while, the outlet temperature of the new CE case remains at the highest with the additional heat internally released from the promoted internal methanation. Also, the amount of internal methanation cannot be too large as well, which will result in too much heat released and unacceptable temperature difference inside the stack.

Therefore, it can be concluded that (1) the internal methanation is an efficient way of directly transferring the methanation heat to maintain high stack temperature, (2) the internal methanation should be well controlled to avoid a large increase in stack temperature, and (3) to maximize internal methanation the stack should be operated with a low current density.

The selection of stack operating points needs to consider the economic viability. The promotion of internal methanation under high-pressure CE has been expected to reduce the sizes and costs of downstream catalytic methanator and upgrading units. However, as discussed above, to have decent internal methanation, the current density

needs to be below 0.5 A/cm^2 for a stack-outlet methane fraction of over 5 vol.% (dry gas) and 0.4 for over 10 vol.%. Compared with the atmospheric CE at a higher current density, the promotion of internal methanation lowers the total methane yield for the same SOE hardware but enhances system efficiency. Therefore, from an economic viewpoint, the use of internal methanation eventually will be a decision considering (1) the reduction of investment costs of downstream processes, (2) the increase in the investments related to the SOE (e.g., the pressure vessel, the increased number of stacks, and the change of stack replacements), and (3) the decrease in operating costs by the reduced electricity consumption due to efficiency improvement.

6. Conclusions

Several fundamental design issues for the co-electrolysis based power-to-methane systems were addressed to identify the benefits and conditions of pressurized operation and internal methanation. The electrolyzer model developed previously in [26] was further improved by introducing the chemical equilibrium for internal methanation and then calibrated with a large set of test data. With the newly calibrated model, the role of CO_2 in co-electrolysis and the difference between the experimental (quasi-isothermal) and practical (quasi-adiabatic) performances were studied. Afterwards, the conditions and extents of pressurized operation and internal methanation were identified from both the stack and system levels. The major conclusions include:

- The co-electrolysis seems to be dominated by the electrochemical split of H_2O , while the CO_2 is converted by chemical reactions inside the stack. The performance worsened by an increased CO_2 feed fraction is due to the increased overpotentials of concentration and cathode activation.
- Practical stack performance might be no better than the experimental. Heat losses worsen the electrochemical performances as

well. Employing the cell/stack performances obtained from isothermal laboratory tests for system design might lead to an over-estimation of system performances.

- Internal methanation can be effectively promoted by enhancing partial-pressure driving force via high pressure and reactant utilization. High sweep-gas feed and low current density are preferred to control the stack temperature for high internal methanation. A high methane fraction at the stack outlet, 30 vol.% (dry gas), might be obtained at 30 bar and 0.3 A/cm^2 with a reactant utilization 80% and an air feed 30 sccm/cm^2 .
- From a system perspective, the maximum-achievable methane fraction inside the stack is lower, 15 vol.% (dry gas) at 15 bar for 0.27 A/cm^2 with 80% reactant utilization and no sweep gas. Without sweep gas, as preferred for high system efficiency, the strongly-exothermic internal methanation needs to be well controlled to avoid too large increase in stack temperature.
- Internal methanation can serve as an internal heat source to maintain high stack temperature, which is especially preferred when the stack is operated with a low current density. With internal methanation, co-electrolysis based power-to-methane can achieve higher system efficiency than the steam-electrolysis based (90% vs 86% on higher heating value or 83% vs 79% on lower heating value with heat and inverter losses).

Acknowledgment

The research leading to these results has received funding from the European Union's Horizon 2020 under grant agreements n° 699892 (ECo, topic H2020-JTI-FCH-2015-1) and n° 731224 (BALANCE, topic LCE-33-2016). T.-E. Lin thanks the Young Scholar Fellowship Program by Ministry of Science and Technology (MOST) in Republic of China, under Grant MOST 108-2636-E-009-012.

Appendix A. Known or estimated parameters for the SOE model

See Tables A.1–A.5.

Table A.1

Mean characteristic lengths of the involved species [63].

	CO	CO_2	H_2	CH_4	H_2O	N_2	O_2
σ	3.69	3.941	2.827	3.758	2.641	3.798	3.467
ϵ	91.7	195.2	59.7	148.6	809.1	71.4	106.7

Table A.2

Parameters used in Eqs. (25)–(28) and (32) to calculate exchange current densities and activation overpotentials. (The values are estimated if references not given.)

Active species	$\beta_{\text{her}}, -$	$\beta_{\text{oe}}, -$	$k, \text{ A/cm}^2$	$E_{\text{act}}, \text{ J/mol}$
H_2	0.7	0.1	130524.762	9.6e4 [43]
CO	0.5	0.1	1e-5	1.31e5 [43]
O_2			76902.899	8.875e4 [43]

Table A.3

Parameters employed in Eqs. (33) and (34) to calculate the saturation pressures.

	Surface type	Source	Eq. num.	$\Gamma, \text{ mol/m}^2$	$\gamma, -$	$k_d, 1/\text{s}$	$E_d, \text{ J/mol}$
CO_2	Nickel	[64]	Eq. (33)	$2.6\text{e}-5$	$1\text{e}-5$	6.447e7	2.598e4
CO	Nickel	[64]	Eq. (33)	$2.6\text{e}-5$	$5\text{e}-1$	3.56e11	1.1127e5
H_2	Nickel	[46]	Eq. (33)	$2.6\text{e}-5$	$1\text{e}-2$	1.453e1	8.812e4
O_2	LSM	[54]	Eq. (34)			4.9e9 atm	2.00e5

Table A.4

Parameters used in Eqs. (35) and (36) to calculate the ohmic overpotential.

	k , S K/m	E , J/mol
Electrolyte ohmic resistance	3.6e5	8.0e4
Interconnect ohmic resistance	5.264e1	4.085e4

Table A.5

Cell geometry employed for model calibration.

Parameter	Symbol	Value
Cell length	L	0.1 m
Cell width	ω	0.08 m
Cathode thickness	δ_{her}	2.20e–4 m
Anode thickness	δ_{oer}	2.0e–5 m
Electrolyte thickness	δ_e	1.2e–5 m
Particle diameter	d_p	3.7646e–7 m
Pore radius	r_g	1.75e–6 m
Cathode porosity	ϵ_{her}	0.309
Anode porosity	ϵ_{oer}	0.4
Cathode tortuosity	τ_{her}	2.5244
Anode tortuosity	τ_{her}	2.5244

Appendix B. Supplementary material

Supplementary data associated with this article can be found, in the online version, at <https://doi.org/10.1016/j.apenergy.2019.05.098>.

References

- [1] European Commission, Roadmap 2050, Policy (April) (2012) 1–9. arXiv:ISBN 978-92-79-21798-2, doi:10.2833/10759. URL <http://www.roadmap2050.eu/>.
- [2] Wind covers 43.6. <https://renewablesnow.com/news/wind-covers-436-of-denmarks-2017-power-demand-596488/>, accessed on 17.12.2018.
- [3] Skov IR, Mathiesen BV. Danish roadmap for large-scale implementation of electrolyzers. Aalborg Universitet; 2017.
- [4] Yao E, Wang H, Wang L, Xi G, Maréchal F. Thermo-economic optimization of a combined cooling, heating and power system based on small-scale compressed air energy storage. *Energy Convers Manage* 2016;118:377–86.
- [5] Yao E, Wang H, Wang L, Xi G, Maréchal F. Multi-objective optimization and exergoeconomic analysis of a combined cooling, heating and power based compressed air energy storage system. *Energy Convers Manage* 2017;138:199–209.
- [6] Chalamala BR, Soundappan T, Fisher GR, Anstey MR, Viswanathan VV, Perry ML. Redox flow batteries: an engineering perspective. *Proc IEEE* 2014;102(6):976–99.
- [7] Waidhas M. Business opportunities for MW electrolysis and related requirements. 1st international conference on electrolysis, Copenhagen, Jun 12–15, 2017. 2017. URL <http://www.ice2017.net/conference/presentations>.
- [8] De Buck P. Energy transition in europe: the case for gas and gas infrastructure. United Nations Conference on Trade and Development, 8th GLOBAL COMMODITIES FORUM, 23–24 April 2018, Geneva. 2018.
- [9] Banerjee A, Wang Y, Diercks J, Deutschmann O. Hierarchical modeling of solid oxide cells and stacks producing syngas via $\text{H}_2\text{O}/\text{CO}_2$ co-electrolysis for industrial applications. *Appl Energy* 2018;230:996–1013.
- [10] Wang L, Chen M, Küngas R, Lin T-E, Diethelm S, Maréchal F, et al. Power-to-fuels via solid-oxide electrolyzer: operating window and techno-economics. *Renew Sustain Energy Rev* 2019;110:174–87.
- [11] <https://www.balance-project.org/>.
- [12] <http://www.eco-soec-project.eu/>.
- [13] BLOOM ENERGY, Bloom energy server es5-250kw (accessed on 28 April 2019). <https://www.bloomenergy.com/datasheets/energy-server-es5-250kw>.
- [14] Almeida S. Aris energy solutions, llc & solidpower: Fuel cells deployment in the u.s; September 2018. https://aenewengland.org/images/downloads/Past_Meeting_Presentations/speaker_4_sa_solidpower_presentation_1_9_2018.pdf.
- [15] SUNFIRE, Sunfire - powerplus (accessed on 28 April 2019). <https://www.sunfire.de/en/products-and-technology/sunfire-powerplus>.
- [16] HELMETH. European Union's Seventh Framework Programme (FP7/2007-2013) for the Fuel Cells and Hydrogen Joint Technology Initiative: Integrated high-temperature electrolysis and methanation for effective power to gas conversion, www.helmeth.eu, accessed 02.04.2017.
- [17] Founti M, Founti M. Power-to-Gas concept and overview of HELMETH project. NTUA Dissemination Event: Energy Storage Technologies: Focus on Power-to-Gas Technology; 2016.
- [18] www.pentagon-project.eu/.
- [19] Wang L, Düll J, Maréchal F, Van herle J. Trade-off designs and comparative exergy evaluation of solid-oxide electrolyzer based power-to-methane plants. *Int J Hydrogen Energy* 2019;44(19):9529–43. <https://doi.org/10.1016/j.ijhydene.2018.11.151> special Issue on Power To Gas and Hydrogen applications to energy systems at different scales - Building, District and National level. URL <http://www.sciencedirect.com/science/article/pii/S0360319918337832>.
- [20] Jensen SH, Sun X, Ebbesen SD, Knibbe R, Mogensen M. Hydrogen and synthetic fuel production using pressurized solid oxide electrolysis cells. *Int J Hydrogen Energy* 2010;35(18):9544–9.
- [21] Bernadet L, Gousseau G, Chatroux A, Laurencin J, Mauvy F, Reytyer M. Influence of pressure on solid oxide electrolysis cells investigated by experimental and modeling approach. *Int J Hydrogen Energy* 2015;40(38):12918–28.
- [22] Bernadet L, Laurencin J, Roux G, Montinaro D, Mauvy F, Reytyer M. Effects of pressure on high temperature steam and carbon dioxide co-electrolysis. *Electrochim Acta* 2017;253:114–27. <https://doi.org/10.1016/j.electacta.2017.09.037>.
- [23] Sun X, Chen M, Jensen SH, Ebbesen SD, Graves C, Mogensen M. Thermodynamic analysis of synthetic hydrocarbon fuel production in pressurized solid oxide electrolysis cells. *Int J Hydrogen Energy* 2012;37(22):17101–10.
- [24] Jensen S, Langnickel H, Hintzen N, Chen M, Sun X, Hauch A, et al. Pressurized reversible operation of a 30-cell solid oxide cell stack using carbonaceous gases. European fuel cell technology & applications conference-Piero Lunghi Conference, Naples. 2017.
- [25] Hansen JB, Christiansen N, Nielsen JU. Production of sustainable fuels by means of solid oxide electrolysis. *ECS Trans* 2011;35(1):2941–8.
- [26] Wang L, Pérez-Fortes M, Madi H, Diethelm S, Maréchal F, et al. Optimal design of solid-oxide electrolyzer based power-to-methane systems: A comprehensive comparison between steam electrolysis and co-electrolysis. *Appl Energy* 2018;211:1060–79.
- [27] Gao J, Liu Q, Gu F, Liu B, Zhong Z, Su F. Recent advances in methanation catalysts for the production of synthetic natural gas. *RSC Adv* 2015;5(29):22759–76.
- [28] Schaaf T, Grüning J, Schuster MR, Rothenfluh T, Orth A. Methanation of CO_2 -storage of renewable energy in a gas distribution system, *Energy. Sustainab Soc* 2014;4(1):2.
- [29] Rönisch S, Schneider J, Matthischke S, Schlüter M, Götz M, Lefebvre J, et al. Review on methanation—from fundamentals to current projects. *Fuel* 2016;166:276–96.
- [30] Wang W, Wang S, Ma X, Gong J. Recent advances in catalytic hydrogenation of carbon dioxide. *Chem Soc Rev* 2011;40(7):3703–27.
- [31] Jalama K. Carbon dioxide hydrogenation over nickel-, ruthenium-, and copper-based catalysts: Review of kinetics and mechanism. *Catal Rev* 2017;59(2):95–164.
- [32] Zhao K, Wang L, Calizzi M, Moio E, Züttel A. In situ control of the adsorption species in CO_2 hydrogenation: Determination of intermediates and byproducts. *J Phys Chem C* 2018;122(36):20888–93.
- [33] Zhao K, Wang L, Moio E, Calizzi M, Züttel A. Identifying reaction species by evolutionary fitting and kinetic analysis: An example of CO_2 hydrogenation in drifts. *J Phys Chem C* 2019.
- [34] Gallandat N, Mutschler R, Vernay V, Yang H, Züttel A. Experimental performance investigation of a 2 kw methanation reactor. *Sustain Energy Fuels* 2018;2(5):1101–10.
- [35] Götz M, Lefebvre J, Mörs F, Koch AM, Graf F, Bajohr S, et al. Renewable Power-to-Gas: A technological and economic review. *Renew Energy* 2016;85:1371–90.
- [36] Schlereth D, Hinrichsen O. A fixed-bed reactor modeling study on the methanation of CO_2 . *Chem Eng Res Des* 2014;92(4):702–12.

- [37] Kiewidt L, Thöming J. Predicting optimal temperature profiles in single-stage fixed-bed reactors for CO₂-methanation. *Chem Eng Sci* 2015;132:59–71.
- [38] Kangas P, Vázquez FV, Savolainen J, Pajarre R, Koukkari P. Thermodynamic modelling of the methanation process with affinity constraints. *Fuel* 2017;197:217–25.
- [39] Turton R, Bailie RC, Whiting WB, Shaeiwitz JA. Analysis synthesis and design of chemical processes. Pearson Education; 2008.
- [40] Biedermann P, Grube T, Höhle B. Methanol as an energy carrier. Zentralbibliothek: Forschungszentrum; 2006.
- [41] Aicart J, Laurencin J, Petitjean M, Dessemont L. Experimental validation of two-dimensional H₂O and CO₂ Co-electrolysis modeling. *Fuel Cells* 2014;3(3):430–47. <https://doi.org/10.1002/fuce.201300214>.
- [42] Aicart J. Modeling and experimental validation of steam and Carbon Dioxide co-electrolysis at high temperature Ph.D. thesis University of Grenoble; 2014.
- [43] Menon V, Fu Q, Janardhanan VM, Deutschmann O. A model-based understanding of solid-oxide electrolysis cells (SOECs) for syngas production by H₂O/CO₂ co-electrolysis. *J Power Sources* 2015;274:768–81.
- [44] Stoots CM, O'Brien JE, Herring JS, Hartvigsen JJ. Idaho national laboratory experimental research in high temperature electrolysis for hydrogen and syngas production Tech. Rep. Idaho National Laboratory (INL); 2008.
- [45] Dittrich L, Foit S, Vinke I, Eichel R-A, de Haart L. Electrochemical tailoring of syngas during high temperature co-electrolysis. 13th European SOFC & SOE Forum (3–6 July 2018) Lucerne, Switzerland. 2018.
- [46] Zhu H, Kee RJ, Janardhanan VM, Deutschmann O, Goodwin DG. Modeling elementary heterogeneous chemistry and electrochemistry in solid-oxide fuel cells. *J Electrochem Soc* 2005;152(12):A2427–40.
- [47] Menon V, Janardhanan VM, Deutschmann O. Modeling of solid-oxide electrolyser cells: From H₂, CO electrolysis to co-electrolysis. *ECS Trans* 2013;57(1):3207–16.
- [48] Suwanwarangkul R, Croiset E, Fowler M, Douglas P, Entchev E, Douglas M. Performance comparison of Fick's, dusty-gas and Stefan-Maxwell models to predict the concentration overpotential of a SOFC anode. *J Power Sources* 2003;122(1):9–18.
- [49] Kong W, Zhu H, Fei Z, Lin Z. A modified dusty gas model in the form of a Fick's model for the prediction of multicomponent mass transport in a solid oxide fuel cell anode. *J Power Sources* 2012;206:171–8.
- [50] Bear J. Dynamics of fluids in porous media. Courier Corporation; 2013.
- [51] Lehnert W, Meusinger J, Thom F. Modelling of gas transport phenomena in SOFC anodes. *J Power Sources* 2000;0–6.
- [52] Iwai H, Yamamoto Y, Saito M, Yoshida H. Numerical simulation of intermediate-temperature direct-internal-reforming planar solid oxide fuel cell. *Energy* 2011;36(4):2225–34.
- [53] Haberman B, Young J. Three-dimensional simulation of chemically reacting gas flows in the porous support structure of an integrated-planar solid oxide fuel cell. *Int J Heat Mass Transf* 2004;47(17–18):3617–29.
- [54] Narasimhaiah G, Janardhanan VM. Modeling CO₂ electrolysis in solid oxide electrolysis cell. *J Solid State Electrochem* 2013;17(8):2361–70.
- [55] Rao M, Sun X, Hagen A. Long term testing of solid oxide electrolysis cells under co-electrolysis conditions. *ECS Trans* 2017;80(9):57–69.
- [56] Rinaldi G, Diethelm S, Oveisi E, Burdet P, Van Herle J, Montinaro D, et al. Post-test analysis on a solid oxide cell stack operated for 10,700 hours in steam electrolysis mode. *Fuel Cells* 2017;17(4):541–9.
- [57] Basu S, Khan AL, Cano-Odena A, Liu C, Vankelecom IF. Membrane-based technologies for biogas separations. *Chem Soc Rev* 2010;39(2):750–68.
- [58] Jensen JO, Vestbø AP, Li Q, Bjerrum N. The energy efficiency of onboard hydrogen storage. *J Alloy Compd* 2007;446:723–8.
- [59] Wang L, Yang Z, Sharma S, Mian A, Lin T-E, Tsatsaronis G, et al. A review of evaluation, optimization and synthesis of energy systems: Methodology and application to thermal power plants. *Energies* 2019;12(73):00. <https://doi.org/10.3390/en12010073>.
- [60] <http://www.sophia-project.eu/>.
- [61] Kotisaari M, Thomann O, Montinaro D, Kiviaho J. Evaluation of a SOE stack for hydrogen and syngas production: a performance and durability analysis. *Fuel Cells* 2016.
- [62] Jeanmonod G, Wang L, Diethelm S, Maréchal F, Van herle J. Trade-off designs of power-to-methane systems via solid-oxide electrolyzer and the application to biogas upgrading. *Appl Energy* 2019;247:572–81. URL <https://www.sciencedirect.com/science/article/pii/S0306261919307020>.
- [63] Hernández-Pacheco E, Singh D, Hutton PN, Patel N, Mann MD. A macro-level model for determining the performance characteristics of solid oxide fuel cells. *J Power Sources* 2004;138(1):174–86.
- [64] Janardhanan VM, Deutschmann O. CFD analysis of a solid oxide fuel cell with internal reforming: Coupled interactions of transport, heterogeneous catalysis and electrochemical processes. *J Power Sources* 2006;162(2):1192–202.